3

Chemical Force Microscopy Nanoscale Probing of Fundamental Chemical Interactions

Aleksandr Noy, Dmitri V. Vezenov, and Charles M. Lieber

1 Basic Principles of Chemical Force Microscopy

1.1 Chemical Sensitivity in Scanning Probe Microscopy Measurements

Intermolecular forces impact a wide spectrum of problems in condensed phases: from molecular recognition, self-assembly, and protein folding at the molecular and nanometer scale, to interfacial fracture, friction, and lubrication at a macroscopic length scale. Understanding these phenomena, regardless of the length scale, requires fundamental knowledge of the magnitude and range of underlying weak interactions between basic chemical functionalities in these systems (Figure 1). While the theoretical description has long recognized that intermolecular forces are necessarily microscopic in origin, experimental efforts in direct force measurements at the microscopic level have been lagging behind and have only intensified in the course of the last decade. Atomic force microscopy (AFM)[1,2] is an ideal tool for probing interactions between various chemical groups, since it has pico-Newton force sensitivity (i.e., several orders of magnitude better than the weakest chemical bond[3]) and sub-nanometer spatial resolution (i.e., approaching the length of a chemical bond). These features enable AFM to produce nanometer to micron scale images of surface topography, adhesion, friction, and compliance, and make it an essential characterization technique for fields ranging from materials science to biology.

As the name implies, intermolecular forces are at the center of the AFM operation. However, during the routine use of this technique the specific chemical groups on an AFM probe tip are typically ill-defined. To overcome this inherent limitation of the AFM, Lieber and coworkers introduced the concept of chemical modification of force probes to make them sensitive to specific molecular interactions[4]. By using chemically-functionalized tips, a force microscope can be transformed into a tool that can (i) quantify forces between different molecular groups, (ii) probe surface free energies on a nanometer scale, (iii) determine pK_a values of the surface acid/base groups locally, and (iv) map the spatial distribution of specific functional groups and their ionization state. This ability to discriminate between chemically distinct functional groups has led the Lieber group to name the variation of force microscopy carried out with specifically functionalized tips "chemical force microscopy" (CFM)[4].

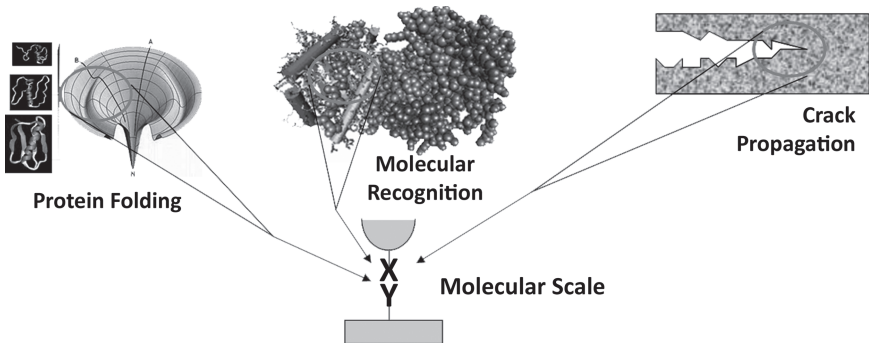

Figure 1. Molecular-scale view of the different examples of condensed phase phenomena illustrating the importance of intermolecular interactions.

1.2 Measuring Interaction Forces with an Atomic Force Microscope

A typical force microscope consists of an integrated cantilever-tip assembly interacting with the sample surface, a detector that measures the displacement of the cantilever and feedback electronics to maintain a constant imaging parameter such as tip-sample separation or force (Figure 2). The integrated cantilever-tip assemblies can have single or V-shaped beams[5] and normal spring constants, k_z, in the range of 0.01–100 N/m. By far, the most popular and versatile detection scheme in AFM is optical lever deflection.[6] In this scheme, the vertical displacement due to normal forces and lateral twist due to friction of the cantilever are measured using a quadrant photodiode, as shown in Figure 2. Force values are determined from the normal displacement, Δz, of the cantilever from its rest position. With an instrumental sensitivity on the order of 0.1 Å, minimal forces in the range of 10^{-13}–10^{-8} N (depending on the cantilever stiffness) can be measured. Hence, AFM can in principle measure molecular interactions ranging from weak van der Waals ($<10^{-12}$ N) to strong covalent (10^{-7} N) bonds.[7–9] In practice, the displacement (and corresponding force) sensitivity is limited by thermally excited cantilever vibrations, optical and electronic noise.[10] If the measurements are conducted in ambient air or liquids, the thermal noise is especially important. For example, cantilever quality factors drop from 10^3-10^5 in vacuum to 10^0-10^2 in fluids due to hydrodynamic damping. The thermal noise limited minimal force is then on the order of 1–20 pN at room temperature. Use of specially designed small cantilevers for AFM can push the force detection threshold to even lower values.[11,12]

AFM measures the magnitude of intermolecular interactions by performing a force-distance measurement, commonly referred to as an F-D curve or simply as a "force curve" (Figure 3). In these measurements, the deflection of the cantilever is recorded during the sample approach-withdrawal cycle.[10] The magnitude of the jump in the retraction trace corresponds to the adhesion between functional groups on the tip and sample surfaces. The observed deflection of the cantilever is converted into a force of adhesion using the cantilever spring constant.

The sphere-on-flat tip-sample geometry of the typical AFM force measurement does not correspond to the interaction between two molecules, as shown in Figure 1. However, the general features of the interaction potential are the same; that is, the potential has a minimum and increases nonlinearly from this minimum (Figure 3). If the cantilever were infinitely stiff, the probe deflection would have simply traced the gradient of the interaction potential (of course, an infinitely stiff cantilever would not have generated any measurable deflection, making such an experiment fairly useless). In practice, the molecular force gradients are higher than the stiffness of the typical cantilevers over a substantial part of the intermolecular force profile; therefore, most AFM cantilevers experience mechanical

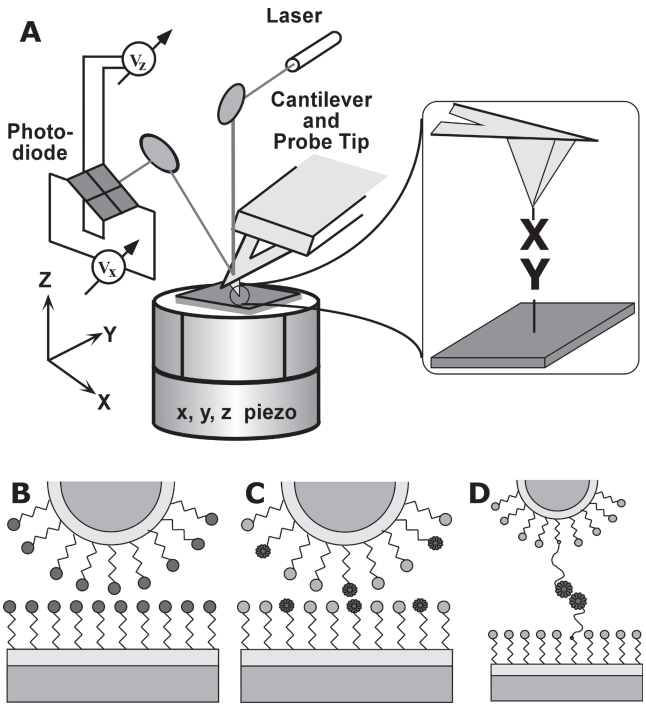

Figure 2. (A) Schematics of the atomic force microscope. The inset shows a close-up of the interactions of the probe and sample surfaces modified with specific functional groups. (B-D) Possible configurations of probe tip and sample functionalization. (B) All terminal functionalities bear the same chemical groups. (C) Active functional groups (red) on the tip are "diluted" with inactive spacer molecules (grey). (D) Interacting groups are attached to the surfaces of tip and sample through long flexible polymer tethers.

instabilities during the force curve cycle. Whenever tip-surface force gradient exceeds the cantilever spring constant, the probe will jump in and out of contact with the sample surface (Figure 3). The magnitude of the adhesion force, which corresponds to the jump out from the potential minimum, is measured precisely in these experiments. Several recent developments have also attempted to use the AFM to map the entire interaction potential (see the chapter by P. Ashby for a detailed discussion of these efforts).

1.2.1 CFM and Other Force Spectroscopy Techniques

CFM is not unique in its ability to measure interactions between molecules and molecular assemblies; other techniques such as the surface forces apparatus (SFA)[13], an elastomer lens-on-plate (or "JKR") apparatus[14,15], colloidal probe microscope[16,17], interfacial force microscope[18], and optical tweezers[19] have also been successful in probing molecular-scale forces. Yet AFM-based techniques hold the distinction of being able to probe specific interactions on surfaces *locally*, thus having the ability to combine quantitative intermolecular force measurements with high-resolution imaging.

1.3 AFM Tip Modification with Chemical Functional Groups

General strategies for modification of the AFM probe tips with different chemical functionalities are covered extensively in the chapter 7; therefore, we will only briefly touch upon the basic strategies of probe functionalization for CFM measurements. To probe

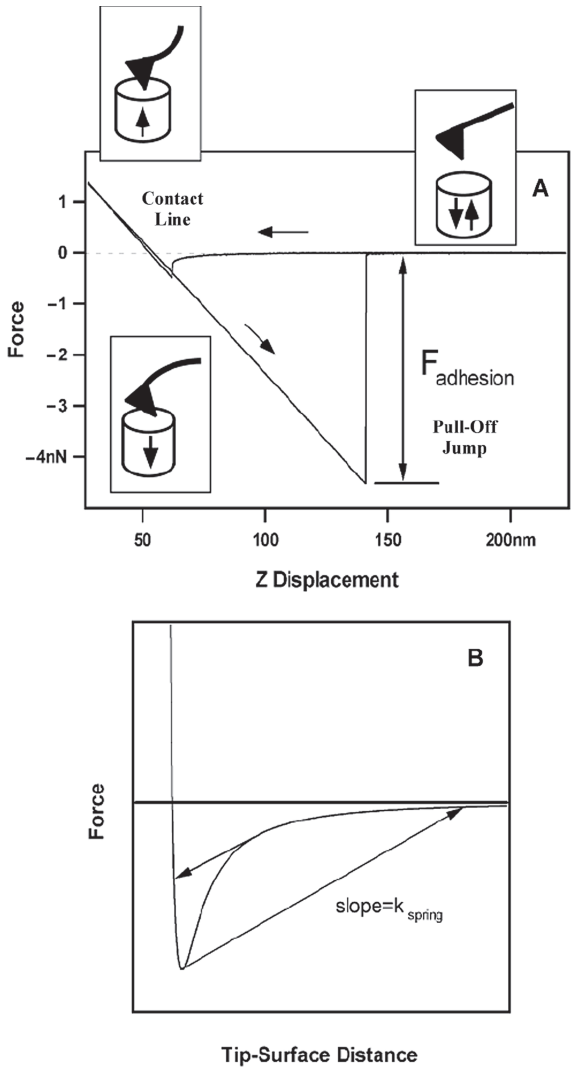

Figure 3. (A) Typical force-vs-Z-piezo displacement curve. At large separations, no force is observed between tip and sample. At short distances, the van der Waals attraction will pull the tip abruptly into contact with the sample (jump into contact point). After that, the deflection of the soft cantilever tracks the movement of the sample (linear compliance regime). Hysteresis in the force between tip and sample is observed when the tip is withdrawn from the sample. The finite force necessary to pull the tip off the sample surface corresponds to the adhesive force between functional groups on the surfaces of the tip and sample. (B) The cycle in (A) is shown as a schematic intermolecular potential between the tip-sample functional groups. Whenever the force gradient exceeds the cantilever spring constant k_{spring} the system becomes mechanically unstable and cantilever jumps occur.

interactions between functional groups in a rationally controlled manner, we need to modify the probes with well defined molecular layers. The simplest way that this modification can be accomplished is by using monolayers of amphiphilic molecules chemisorbed on the surface of the tip. Different types of interactions can then in principle be studied by varying the head group of the amphiphile.

By far the most well developed approach involves self-assembly of monolayers (SAMs) of functionalized organic thiols onto the surfaces of Au-coated Si_3N_4 or Si tips.

Stable, robust, and crystalline monolayers of alkyl thiols or disulfides containing a variety of terminal groups are a staple of the surface science literature and are readily prepared[20–25]. Using systems of thiol SAMs on Au, systematic studies have been carried out on the interactions between basic chemical groups on the probe tip and similarly modified Au substrates.[4, 26–37] Covalent modification of AFM probes with reactive silanes or through direct Si-C bond formation has also been reported.[102–104]

1.4 Role of Environment in CFM Experiments: Experiment Design and Basic Types of Detectable Forces

The environment, in which surfaces interact, plays a crucial role in determining the nature and the magnitude of measured forces (Figure 4). To probe interactions determined solely by solid surface free energies (i.e., bare functional groups), we need to measure adhesion forces in vacuum. These measurements (Figure 4A) would admittedly be the easiest to compare with the available body of the computational literature; but unfortunately more often than not these measurements have very little to do with the real systems in which the functional groups are exposed to the ambient environment or immersed in water or other liquid medium. Force measurements carried out in ambient air (Figure 4B) are much more relevant to the practical applications, yet they are also much more difficult to interpret. The major contribution to the interactions in ambient air (and the major obstacle to consistent data interpretation) comes from capillary forces generated by the meniscus forming between the AFM probe and sample surfaces (Figure 4C). These forces[8, 38, 39] are usually 1–2 orders of magnitude higher than specific chemical interactions, and thus they almost always obscure the relatively small differences in molecular forces between tip and sample functional groups. We also note that capillary condensation will emphasize the relative degree of wetability (hydrophilicity) and can serve as a basis for discriminating between hydrophobic and hydrophilic groups when

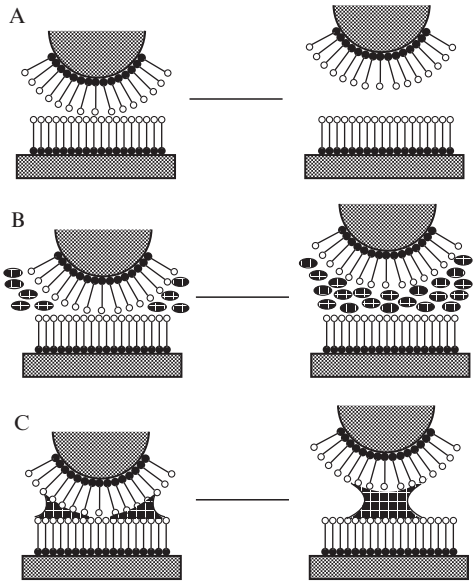

Figure 4. Comparison between force measurements in ultrahigh vacuum, liquids, and ambient air. (A) Interactions under high vacuum conditions are determined by solid surface free energies. (B) Pulling apart the surfaces under liquid will result in their solvation upon separation. The magnitude of the adhesion force is defined by solid-liquid surface free energies. (C) Experiments conducted under ambient conditions reflect the wettability of the surfaces, since the predominant interaction results from capillary forces.

imaging under ambient conditions.[40] Measurements performed in a dry inert gas atmosphere may seem an attractive approach to circumventing the limitations imposed by capillary forces;[41] however, researchers should use extreme caution in interpreting the results of these experiments, since it is difficult to exclude or account for the presence of adsorbed vapor on high energy surfaces.

The only general approach for eliminating the capillary effect is to conduct the experiments in liquid rather than in air.[42] In this case adhesion force measurements with both surfaces immersed in liquid will reflect the interplay between surface free energies of *solvated* functional groups. In addition to introducing the solvation energy components into the overall energy balance of the system, the presence of tightly-bound solvation layers on the interacting surfaces can introduce effects reminiscent of the collective ("hydrophobic") interactions, and further complicate interpretation of the results (the end of this chapter presents a more detailed discussion of these effects). Understanding fundamental interactions in aqueous solutions is especially important, since AFM has become a routine technique for probing and imaging biological systems.[43–54]

1.5 Making Sure that CFM Experiments Work: Characterization and Calibration of Force Probes and the Force Microscope

To obtain absolute force values and make direct comparisons between studies requires knowledge of the cantilever spring constants and the tip radii. Researchers have introduced several approaches for experimental calibration of normal spring constants of the AFM cantilevers, k_z,[55–58] yet the thermal resonance method[56] has become the dominant technique. Current generation commercial AFMs make calibration of the individual tips easier than ever by incorporating automated calibration routines directly into the microscope control software. As the process variations during mass-fabrication of the AFM cantilevers could introduce up to 50% deviations in the cantilever spring constants for nominally identical cantilevers, with additional changes in effective stiffness due to gold coating,[26] *individual calibration of every cantilever used for force spectroscopy measurements is imperative*. The lateral spring constants k_L of cantilevers can also be determined experimentally[59] or derived using the corresponding normal spring constants through the cantilever geometry.[26, 60–62]

In addition, the sensitivity of the optical detector, which measures the cantilever displacement, must be calibrated to obtain absolute forces. The normal (z) sensitivity of the detector can be readily determined from the linear compliance region of the force curve when the tip is pushed against a stiff sample (Figure 3A); the literature also contains examples of noncontact methods.[63, 64] The lateral (xy) sensitivity of the detector in the past was frequently calibrated from atomic stick-slip friction loops,[65] although implicit neglect of the lateral stiffness of the contact could introduce a significant error. A more robust, but more involved, procedure than the use of stick-slip friction loops requires a standard with two different well defined surface slopes. It is also possible to relate the normal sensitivity of a detector to its lateral sensitivity.[63, 66, 67]

Finally, the tip radius is an important parameter to characterize, since it affects the contact area between the tip and the sample; that is, the number of molecular contacts. Three methods for tip characterization have been applied in CFM: 105(i) tip imaging using scanning electron microscopy (SEM), which provides a direct measure of the radius and is the most common approach; (ii) the "adhesion standard" system (e.g., CH_3-H_2O-CH_3), which provides the benchmarked work of adhesion to define effective tip radius using measured adhesion force, known work of adhesion, W_{132}, and a selected contact mechanics model, e.g., $R = F_a/(1.5\pi W)$; (iii) tip shape reconstruction algorithms, which can generate the probe tip shape from the AFM images of a tip characterizer, such as sharp Si spikes on a flat surface, atomically sharp features on the (305) face of $SrTiO_3$, colloidal gold clusters, or even random sharp features on the sample. In at least one test, blind tip shape restoration (method iii)

produced tip radius values that were in excellent agreements with the estimates from the direct SEM imaging of the probes (method i).[106]

2 Probing Specific Nanoscale Interactions with CFM

A large number of CFM studies of the interactions between different chemical functional groups covalently linked to tips and samples have appeared since the initial report of CFM.[4, 26] Tables 1 and 2 present some typical results. Adhesion forces between tips and substrates modified with SAMs terminating in CF_3, CH_3, OCH_3, CH_2Br, OH, COOH, $COCH_3$, $CONH_2$, and NH_2 groups have been measured in organic[4, 26, 33] and aqueous solvents,[27] and inert dry atmosphere.[31,68] Even a quick glance through these tables shows that the notion of determining a defined bond strength for a particular functional group pair interaction is too simplistic. Interaction forces measured between the same functionalities in different solvents can differ by almost an order of magnitude; and, even more troubling, measurements performed by different research groups using similar probe functionalization in the same solvent sometimes produce different results. It is clear that the measured interaction force can be influenced by many different parameters. In the following sections we quickly review the observed trends, outline the experimental factors that influence forces in CFM, and present a detailed discussion of the basic concepts that are useful in designing and interpreting CFM experiments.

2.1 CFM in Air and in Gas Environments

Several studies of functional group interactions have been carried out in dry gases[31, 68] and are summarized in Table 1. Several qualitative trends are noticeable. The adhesive forces between tips and samples modified with SAMs that both terminate in nonpolar groups are small[68] or undetectable within the resolution of reported experiment.[31] Observed adhesive forces are also small when one of the SAM surfaces terminates with nonpolar groups and the other with polar groups. In contrast, when both tip and sample SAM surfaces terminate with hydrogen bonding groups (Table 1, entries 1, 4–7) significant adhesion is observed. The relative magnitudes of the adhesive forces are also in accord with the with expected bond strengths; that is, $COOH/NH_2 > COOH/COOH > NH_2/NH_2$. Note that the use of dried gases is not sufficient to completely preclude adsorption of water and other species on the surfaces of SAMs. Hence, to determine unambiguously the magnitudes of the interactions between bare molecular assemblies, it is necessary to carry out CFM studies under ultrahigh vacuum conditions, which can ensure clean surfaces.

Table 1. Adhesion Forces Between Functional Groups in Gaseous Environment.

Functional Group (Tip-Surface)	Monolayer, Chain Length	Medium	Adhesion (nN)	Ref.
COOH-COOH	thiol SAM, C_{16}	dry Ar	62	31
COOH-CH_3	thiol SAM, C_{16}	dry Ar	≈0	31
CH_3-CH_3	thiol SAM, C_{18}	dry Ar	≈0	31
NH_2-COOH	thiol SAM, C_{11}	dry N_2	4.3±0.4	68
COOH-COOH	thiol SAM, C_{11}	dry N_2	1.4±0.3	68
NH_2-NH_2	thiol SAM, C_{11}	dry N_2	0.7±0.2	68
CH_3-CH_3	thiol SAM, C_{11}	dry N_2	0.4±0.2	68

2.2 CFM in Organic Solvents

Initial CFM experiments carried out in organic solvents focused on probing van der Waals and hydrogen bonding interactions, while CFM performed in electrolyte solution assessed hydrophobic and electrostatic forces (Table 2). Representative F-D curves obtained in ethanol using Au-coated tips and samples that were functionalized with SAMs terminating in either CH_3 or COOH groups readily reveal the difference between the individual interactions (Figure 5A). To quantify the differences and uncertainties in the adhesive interactions between different functional groups, however, it is always necessary to record multiple force curves for each type of intermolecular interaction and each tip-sample pair. Histograms of the observed adhesion forces typically exhibit Gaussian distributions (Figure 5B) and yield mean adhesion forces (± its experimental uncertainty) of 2.3 ± 0.8, 1.0 ± 0.4, and 0.3 ± 0.2 nN for interactions between COOH/COOH, CH_3/CH_3, and CH_3/COOH

Table 2. Interaction strength between AFM tips and samples functionalized with specific functional groups measured in different solvents.

Functionality	Probe functionalization monolayer	Solvent	Adhesion (nN)	Reference
CH_3-CH_3	Silane, C_2	EtOH	0.4 ± 0.3	29
CH_3-CH_3	Silane, C_9	EtOH	0.7 ± 0.6	29
CH_3-CH_3	Silane, C_{14}	EtOH	2.4 ± 1.2	29
CH_3-CH_3	Silane, C_{18}	EtOH	3.5 ± 2.3	29
CH_3-CH_3	Thiol, C_{18}	EtOH	1.0 ± 0.4	26
CH_3-CH_3	Thiol, C_{12}	EtOH	2.3 ± 1.1	33
CF_3-CF_3	Silane, C_{10}	EtOH	15.4	30
CH_3-CF_3	Silane, C_{18}, C_{10}	EtOH	*repulsive*	30
CH_3-CH_3	Silane, C_{18}	$CF_3(CF_2)_6CF_3$	52	30
CF_3-CF_3	Silane, C_{10}	$CH_3(CH_2)_6CH_3$	21	30
CH_3-CH_3	Thiol, C_{12}	$CH_3(CH_2)_{14}CH_3$	0.07 ± 0.05	33
COOH-COOH	Thiol, C_{11}	$CH_3(CH_2)_{14}CH_3$	0.11 ± 0.02	33
COOH-COOH	Thiol, C_{11}	Hexane	0.95 ± 0.26	101
COOH-CH3	Thiol, C_{11}, C_{18}	EtOH	0.3 ± 0.2	26
COOH-COOH	Thiol, C_{11}	EtOH	2.3 ± 0.8	26
COOH-COOH	Thiol, C_{11}	EtOH	0.27 ± 0.04	33
COOH-COOH	Thiol, C_{11}	PrOH	1.37 ± 0.26	101
CH_2OH-CH_2OH	Thiol, C_{11}	EtOH	0.18 ± 0.18	33
COOH-COOH	Thiol, C_{11}	Water	2.8 ± 0.2	101
COOH-COOH	Thiol, C_{11}	Water,	7.0 ± 0.2	27
COOH-COOH	Thiol, C_{11}	pH < 5	2.3 ± 1.1	33
COOH-CH_2OH	Thiol, C_{11}	Water, DI	1.1 ± 0.5	27
CH_2OH-CH_2OH	Thiol, C_{11}	Water, pH < 5	1.0 ± 0.2	27
CH_2OH-CH_2OH	Thiol, C_{11}	Water,pH < 5	0.3 ± 0.05	33
CH_3-CH_3	Thiol, C_{18}	Water, DI	60 ± 5	27
CH_3-CH_3	Thiol, C_{12}	Water	12.5 ± 4.4	33

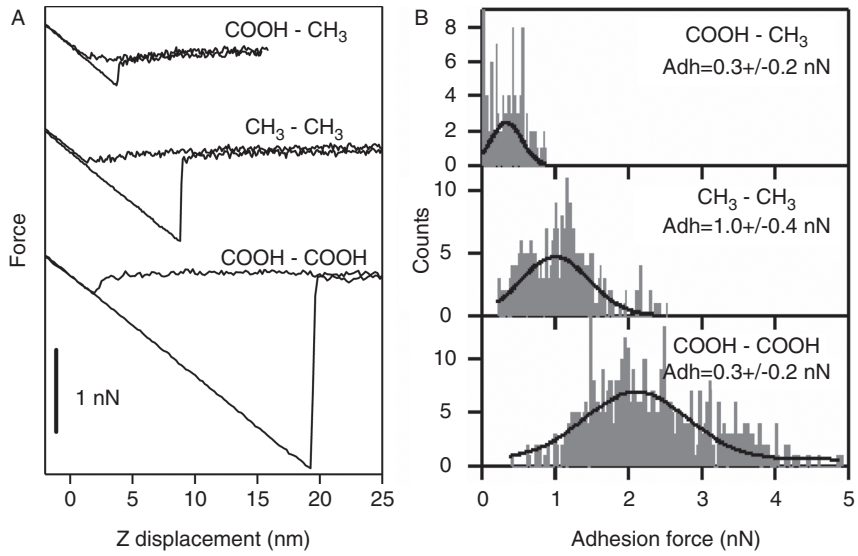

Figure 5. Specific interactions between basic chemical functionalities in ethanol. (A) Representative force vs. distance traces recorded between samples and tips functionalized with simple organic functional groups.[4] (B) Histograms of adhesion forces recorded between similar tip/sample pairs in repeated measurements. Solid lines indicate Gaussian fits to the data.[26]

groups, respectively. Since the mean values do not overlap, it is possible to differentiate between these chemically distinct functional groups by measuring the adhesion forces with a tip that terminates in a defined functionality. The observed trend in the magnitudes of the adhesive interactions between tip/sample functional groups, i.e., COOH/COOH > CH_3/CH_3 > CH_3/COOH, agrees with the qualitative expectation that interactions between hydrogen bonding groups (i.e., COOH) will be greater than between non-hydrogen bonding groups (i.e., CH_3).

When the solvent is chemically similar to the tip and sample terminal functional groups (for example, CH_3 groups in hexadecane or CH_2OH groups in ethanol), the forces required to separate the tip and surface are small (Table 2). Cross-interactions between immiscible components were found to be either very small (e.g., CH_3/COOH in ethanol) or even repulsive (e.g., CH_3/CF_3 in ethanol). In contrast, when the solvent is immiscible with the functional groups that terminate the SAMs on the tip and sample, the adhesive forces are extremely large. Both van der Waals (Table 2 CH_3 groups in perfluorohexane or CF_3 groups in hexane) and hydrophobic (Table 2 CH_3 groups in water) interactions can be responsible for this latter behavior.

3 Interpretation of CFM Experiments

3.1 Thermodynamic Model: Surface Free Energies and Surface Tension Components Models

3.1.1 Contact Mechanics Approach to Tip-Surface Contact in CFM

Although force microscopy with sharp probes approaches the limit of point contact, in practice the number of interacting molecular species in CFM experiments remains on the order of tens to hundreds. Energies of intermolecular interactions and the number of functional groups contributing to experimentally observed forces can be derived from adhesion data by considering the contact deformation between the probe and a surface.

The problem of adhesive contact between the tip of radius R_1 and sample of local curvatures R_2 can be treated in terms of elastic contact between a flat surface and a sphere of effective radius R:

$$R = (1/R_1 + 1/R_2) \tag{1}$$

The sphere deforms due to both repulsive forces (Born repulsion) within the area of contact and attractive forces near the edge of the contact zone and outside it. The interatomic distances within the contact zone differ little, and this area can be considered to be a flat circle of radius a. For repulsive-only interactions (hard-wall potential, Hertz model), the dependence of the contact area size on external load P is well known:

$$a^3 = \frac{RP}{K}, \tag{2}$$

$$\text{where } K = \frac{4}{3}\left(\frac{1-\nu_1^2}{E_1} + \frac{1-\nu_2^2}{E_2}\right)^{-1} \tag{3}$$

is the effective elastic constant of the system (ν is the Poisson ratio and E is the Young's modulus). Realistic potentials are not straightforward to implement in the models of contact mechanics, because interaction force depends on the intermolecular separation, in other words, it is defined by the surface profile of the deformed sphere, which in turn depends on the interaction force. One can decouple the force-surface profile dependency by assuming that i) the profile is not changed because of the presence of attractive forces outside the contact zone, or ii) attractive forces act only within the contact area (zero range forces).

The first option means that the forces are based on the Hertz result and leads to the DMT (Derjaguin, Muler, and Toporov) model of adhesion:[69] the radius *a*, the surface profile, and the stress distribution are given by Hertz equations with the external load substituted by the total force $P + F_a$, which includes adhesion F_a. The force of adhesion can then be related to the thermodynamic work of adhesion by summing up interactions in the gap between the surfaces outside the contact zone,

$$a^3 = \frac{RP_1}{K} \qquad P_1 = P + 2\pi W_{132} \qquad F_a = 2\pi R W_{132} \tag{4}$$

The work of adhesion for separating the sample and tip gives the balance of interfacial free energies $W_{132} = \gamma_{13} + \gamma_{23} - \gamma_{12}$. The second choice, implemented in the JKR (Johnson, Kendall, and Roberts) model[70], results in a different stress distribution: compressive in the center of the contact zone, changing to tensile when approaching the boundary (and zero outside the contact circle). The total energy of the system is minimized when the external load P is substituted by an apparent load P_1:

$$a^3 = \frac{RP_1}{K} \qquad P_1 = P + 3\pi W_{132} R + \sqrt{6\pi W_{132} RP + \left(3\pi W_{132} R\right)^2} \qquad F_a = \frac{3}{2}\pi R W_{132} \tag{5}$$

The two models differ substantially in predicted contact area, force of adhesion, and surface profile. JKR theory predicts a finite radius of contact under zero external load and when surfaces separate: $a_{0(JKR)} = \left(\frac{6\pi W_{132} R^2}{K}\right)^{1/3}$ and $a_{s(JKR)} = \frac{a_{0(JKR)}}{4^{1/3}} \approx 0.63 a_{0(JKR)}$, respectively. One can estimate the number of molecular contacts in adhesive interactions by dividing the contact area at pull-off, a_s, by the area occupied by a single functional group. Corresponding quantities

for DMT theory are $a_{0(DMT)} = \left(\frac{2\pi W_{132} R^2}{K}\right)^{1/3}$ and $a_{s(DMT)} = 0$. The estimate of the number of molecular contacts in the DMT model must consider the range of intermolecular forces z_0.

A self-consistent approach to the contact problem typically requires numerical solutions. Such calculations based on the Lennard-Jones potential showed[71] that the DMT and JKR results correspond to the opposite ends of a spectrum of a non-dimensional parameter (so-called Tabor elasticity parameter):

$$\mu = \left(\frac{16}{9}\frac{RW^2}{K^2 z_0^3}\right)^{1/3} \tag{6}$$

This parameter asserts the relative importance of the deformation under surface forces: for $\mu < 0.1$ the DMT model is appropriate, for $\mu > 5$ the JKR model applies. Although the JKR model predicts infinite stresses at the perimeter of the contact zone, whereas DMT model predicts discontinuous stress, numerical results did not display any abnormal stress distributions.

To avoid self-consistent calculations based on a specific potential, Maugis derived an analytical solution to the adhesive contact problem[72] by using the Dugdale approximation that the adhesive stress has a constant value σ_0 (theoretical stress) until a separation $h_0 = W/\sigma_0$ is reached at radius c, whereupon it falls to zero (Figure 6). The net normalized force is given by (m = c/a):

$$\bar{P} = \bar{a}^3 - \lambda\bar{a}^2\left(\sqrt{m^2-1} + m^2 \arccos(1/m)\right), \tag{7}$$

where parameter λ is a measure of the ratio of the elastic deformation to the range of surface forces and $\bar{a}$ and $\bar{P}$ are the scaled radius of the contact zone and external load:

$$\lambda = 2\sigma_0\left(\frac{RK^2}{\pi W}\right)^{1/3} = 1.16\mu \quad \bar{a} = \frac{a}{\left(\pi WR^2/K\right)^{1/3}} \; \bar{P} = \frac{P}{\pi WR} \tag{8}$$

The elasticity parameter λ is related to m through:

$$\frac{1}{2}\lambda\,\bar{a}^2\left[(m^2-2)\arccos(1/m) + \sqrt{m^2-1}\right] + \frac{4}{3}\lambda^2\bar{a}$$
$$\left[\sqrt{m^2-1}\arccos(1/m) - m + 1\right] = 1. \tag{9}$$

When λ is increased, $m \to 1$ (i.e., contact forces only, $c = a$) and the JKR limit is recovered:

$$\bar{P} = \bar{a}^3 - \sqrt{6\bar{a}^3} = \bar{P}_1 - \sqrt{6\bar{P}_1}. \tag{10}$$

When λ is decreased, $m \to \infty$ (i.e., long-ranged forces, $c >> a$) and the DMT limit is achieved:

$$\bar{P} = \bar{a}^3 - 2. \tag{11}$$

The Maugis-Dugdale (MD) model is an accurate representation of the adhesion in the presence of a liquid meniscus (constant pressure inside the meniscus).

The choice of a functional form of the contact area dependence on the external load is crucial to interpretation of the friction forces, which will depend on both the interfacial shear strength of the contact and its size. The difficulty with MD theory is that it does not easily lend itself to fitting the experimental data. This issue was addressed by Carpick et al.,[73] who demonstrated that a simple general equation:

$$\frac{a}{a_{0(\alpha)}} = \left(\frac{\alpha + \sqrt{1 - P/F_{a(\alpha)}}}{1+\alpha} \right)^{2/3} \tag{12}$$

closely approximates Maugis' solution and can be used to fit experimental data onto a contact area (friction). Numerical results are then used to obtain the Tabor parameter from the fitting parameter α ($\alpha = 0$ corresponds to DMT case, $\alpha = 1$ corresponds to JKR case).

The exact value of the numerical coefficient in Equation 4 and 5 for F_a (3/2 vs. 2) is beyond the experimental uncertainty of CFM experiments (widths of adhesion force distributions plus errors in determination of k and R, see Tables 1 and 2); and both approaches can and have been used to derive surface free energies from adhesion data. On can construct an "adhesion map" of the applicability of particular models depending on the parameter μ and applied force.[74] In the CFM, high modulus materials (≈100 GPa) and tip radii ≈100 nm result in $\mu < 1$; thus CFM experiments fall into a "transition" zone. Numerical calculations for $\mu < 0.3$ indicate, however, that the compliance of adhesive contact and computed contact radii are still well represented by the JKR equations. Therefore, it appears that JKR equations give good predictions even under conditions well outside the expected JKR zone. We note that it is impossible to place a given system in the respective contact mechanics regime based on the adhesion force measurement alone, since contact area is not measured independently in CFM. An estimate of the Tabor elasticity parameter is preferred in this case, although this approach still needs to make assumptions about effective elastic constant of the monolayer/substrate system.

3.1.3 Intermolecular Force Components Theory

The sphere-on-flat tip-sample geometry of the AFM does not correspond to the interaction between two atoms or molecules. The Lennard-Jones potential typically used to represent interaction between molecular species (with minimum energy ε_0):

$$\frac{F_{molec}(z)}{\varepsilon_0 / z_0} = 12 \left[-\left(\frac{z}{z_0} \right)^{-7} + \left(\frac{z}{z_0} \right)^{-13} \right] \tag{13}$$

has to be modified for the CFM geometry to account for multiple intermolecular pairs. The fundamental $1/z^7$ law of attraction for dispersion forces between molecules was first derived by London based on second order perturbation theory. An alternative approach by Dzyaloshinskii, Lifshitz, and Pitaevskii[75] uses quantum field theory to relate van der Waals (vdW) forces to spectroscopic properties of materials, but produces an analytically useful result only in the case of vdW pressure between two semi-infinite dielectric slabs separated by a third medium:

$$f(z) = -\frac{A}{6\pi} \frac{1}{z^3} \tag{14}$$

where A is the (non-retarded) Hamaker coefficient, which relates to a detailed dielectric behavior of the materials through a complete electromagnetic spectrum.

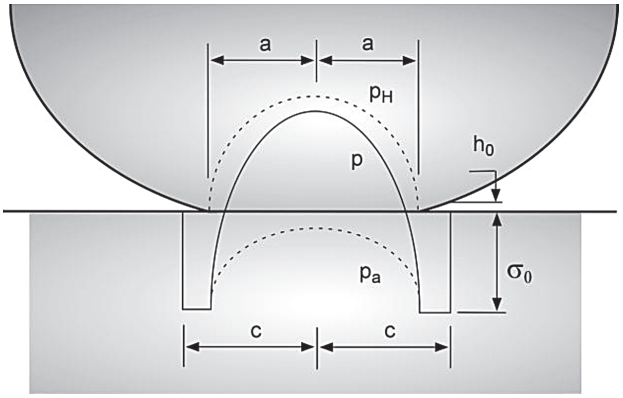

Figure 6. The Maugis-Dugdale stress distribution is a sum of two terms: the Hertz pressure p_H acting on the area of radius a, and adhesive tension p_a acting on the area confined by radius c.

The two scales (macro and molecular) converge in Hamaker's approach: from the power law for intermolecular interactions, $F_{molec}(z) = -C/z^7$, the macroscopic van der Waals force between bodies 1 and 2 with molecular densities ρ_1 and ρ_2 can be obtained by volume integration of the pair-wise interactions:

$$f(z) = -\frac{\pi\rho_1\rho_2 C}{36z^3}, \text{where } \rho_1\rho_2 C = 6A/\pi^2 \tag{15}$$

Thus, London's result for interactions across vacuum (α is atomic polarizability)[76]:

$$U_{molec} = -\frac{3}{4\pi} h \frac{\nu_{e1}\nu_{e2}}{\nu_{e1}+\nu_{e2}} \frac{\alpha_1\alpha_2}{z^6} \tag{16}$$

leads to a geometrical mean combining rule for the corresponding Hamaker coefficients ($\nu_{e1} \approx \nu_{e2}$, $\rho_1 \approx \rho_2$) and for the surface free energies in the case of Lifshitz–van der Waals (LW) forces:

$$A_{12} = \pm\sqrt{A_{11}A_{22}} \text{ and } \gamma_{12}^{LW} = \sqrt{\gamma_1^{LW}\gamma_2^{LW}} \tag{17}$$

The pull-off forces, as described in the contact mechanics models, depend on the surface free energies through the thermodynamic work of adhesion. In associating solvents and for polar surfaces, it is important to take a proper account of both additive (symmetric) van der Waals interactions and complementary (asymmetric) electron donor-acceptor interactions (hydrogen bonding). Donor-acceptor or Lewis acid-base interactions are short-ranged (contact) forces and are not accounted for in London's or Lifshitz's treatments of weak intermolecular forces. These interactions, however, influence thermodynamic data, and thus must be included in computational models for analysis and prediction of physicochemical properties—for example, in solvation models and the linear free energy relationship approaches.

Hydrogen bonding interactions operate over the background of the omnipresent dispersion forces. While the dispersion forces for dielectrics are often very similar in magnitude, the hydrogen bonding interaction differentiates various classes of organic functional groups quite dramatically. One can compare, for example, boiling points of homologous hydrocarbons and alcohols or adhesion forces between CH_3/CH_3 and COOH/COOH pairs.

A successful scale of the strength of acid-base interactions was proposed by Fowkes, van Oss, Chaudhury, and Good (FOCG),[77] who recognized the need for having two values to describe the polar surface tension component: one representing electron accepting and the other representing electron donating abilities in combining relations. In this model, the total surface tension of a polar system is separated into van der Waals, γ^{vW}, and Lewis acid, γ^+; and Lewis base, γ^-, components:

$$\gamma_{\text{total}} = \gamma^{\text{LW}} + \gamma^{\text{AB}} \tag{18}$$

where $\gamma^{\text{AB}} = 2\sqrt{\gamma^+\gamma^-}$. For cross-interactions, the following combing rule applies:

$$\gamma_{12} = \sqrt{\gamma_1^{LW}\gamma_2^{LW}} + \sqrt{\gamma_1^+\gamma_2^-} + \sqrt{\gamma_2^+\gamma_1^-} \tag{19}$$

and the solid-liquid interfacial tension is then given by:

$$\begin{aligned}\gamma_{SL} &= \gamma_{SV} + \gamma_{LV} - 2\left(\sqrt{\gamma_{SV}^{LW}\gamma_{LV}^{LW}} + \sqrt{\gamma_{LV}^+\gamma_{SV}^-} + \sqrt{\gamma_{SV}^+\gamma_{LV}^-}\right) \\ &= \left(\sqrt{\gamma_{SV}^{LW}} - \sqrt{\gamma_{LV}^{LW}}\right)^2 + 2\left(\sqrt{\gamma_{LV}^+\gamma_{LV}^-} + \sqrt{\gamma_{SV}^+\gamma_{SV}^-}\right. \\ &\quad \left. - \sqrt{\gamma_{SV}^+\gamma_{LV}^-} - \sqrt{\gamma_{SV}^-\gamma_{LV}^+}\right)\end{aligned} \tag{20}$$

The interpretation of adhesion measurements in liquids can be complicated if all components are involved in acid-base interactions. Although there is no solid fundamental theoretical basis for applying the geometric mean combining rule for interactions of acid-base type (unlike for van der Waals interactions), the FOCG model is conceptually simple and can be applied successfully to rationalize the trends in adhesion forces observed between organic functional groups of model SAMs or polymer systems in organic liquids.

3.2 Scaling Relationships in CFM Experiments

3.2.1 Experimental Geometry: Surface Roughness and Probe Size Effects

One of the advantages of using nanoscale point probes in adhesion studies is that they drastically lower the requirements for the surface quality necessary to achieve molecularly smooth contact, e.g., the sample does not have to display macroscopic atomically smooth areas. Quasi-equilibrium pull-off forces predicted by the contact mechanics equations discussed in the previous sections should be directly proportional to the effective radius defined by Equation 1. We can immediately recognize, however, that substrate roughness, e.g., local variations in the substrate radius of curvature will affect the magnitude of adhesion. For example, analysis of force and topography maps from the AFM measurements on a chemically homogeneous, hydrophobic sample-silanized etched silicon[78] showed an unambiguous direct correlation between the substrate's local curvature and the force of adhesion.

The width of the adhesion force distribution (σ_F) for a $HS(CH_2)_{15}COOH$/$HS(CH_2)_{15}COOH$ pair in ethanol was halved when the polycrystalline Au substrates were replaced by the single crystalline, annealed Au on mica.[79] Similar observations[80] were reported for the adhesion forces in water (Figure 7) using the same $HS(CH_2)_{19}CH_3$ terminated tip on three $HS(CH_2)_{15}CH_3$ modified substrates: (i) 11-nm sputtered Au film, (ii) 110-nm sputtered Au film, and (iii) annealed Au(111) on mica. Remarkably, Au substrates presenting large areas of the (111) face produced the same mean value of adhesion, while the distribution width was a factor of five smaller. These results suggest that the spread of the local curvature distribution of the substrate could be a primary factor responsible for the width of adhesion force distributions for chemically identical tip-sample combinations.

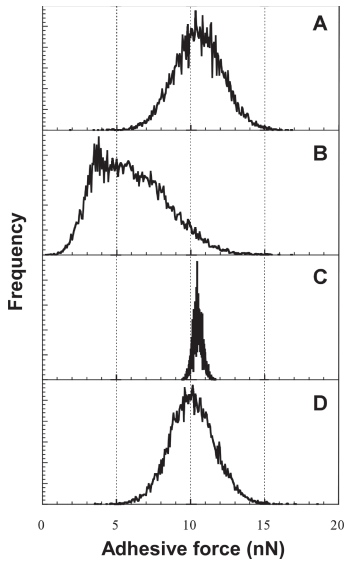

Figure 7. Histograms of adhesive force mappings using the same CH_3-terminated tip on $HS(CH_2)_{19}CH_3$ SAMs formed on: (A) 11 nm thick sputtered gold, (B) 110 nm thick sputtered gold, (C) 100 nm thick thermally evaporated Au(111) on mica, and (D) same as (A). The sequence of CFM measurements was (A)-(B)-(C)-(D).[80]

The most serious practical consequence of varying sample flatness for the interpretation of the chemical force microscopy results is that the measured distributions almost never reflect the inherent statistical distribution width for a given chemical functionality. Thus, statistical treatments of force fluctuations in CFM should be used with caution—a significant contribution to σ_F almost always arises from the fluctuations in the tip-sample contact area due to the differences in local surface curvature.

Scaling of the measured adhesion force values with the size of the contact area and, correspondingly, with the number of bonds comprising the interactions is generally a complicated topic, especially at high loading rates when the kinetic effects are strong[81]. In the quasi-equilibrium limit, some generalizations are possible on the scaling of the adhesion forces with the probe size. The relationship between the tip radius, R, and force of adhesion, F_a, was probed systematically[82] for hydrophobic contacts (CH_3/CH_3) in water. For tip radii ranging from R = 15 nm to R = 125 nm, a remarkably good linear correlation (Figure 8A) existed between the measured adhesion forces and the probe radii.

Moreover, when researchers accounted for substrate roughness (radius of curvature of Au grains) by defining and effective probe radius, the linear fit showed a zero intercept (Figure 8B), as predicted by the contact mechanics models.[82] If we use the value of the thermodynamic work of adhesion in the CH_3-H_2O-CH_3 system of W = 103 mJ/m^2, data in Figure 8 produce a proportionality coefficient of $(1.59 \pm 0.15)\pi W$ between the pull-off force and the effective radius. This value is very close to the $1.5\pi W$ value predicted by the JKR model.

One of the possible solutions to mitigating the effects of the surface roughness on the observed interactions is to use CFM probes of extremely small size. Lieber and co-workers demonstrated an important development in this direction by using chemically-modified carbon nanotube AFM probes for force measurements.[83–85] These probes (especially single-wall carbon nanotube probes) offer a versatile setup for measuring basic chemical

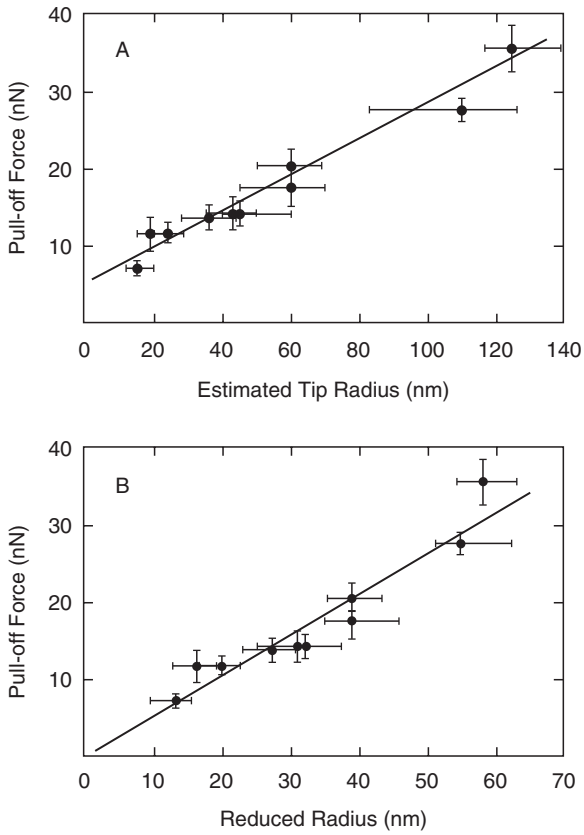

Figure 8. (A) Plot of mean pull-off force vs estimated tip radius (circles) for 10 tips. The solid line shows a linear least squares fit. The vertical error bars represent the standard deviation of the average pull-off force while the horizontal error bars are estimated maximum and minimum radius. (B) Plot of mean pull-off force vs reduced tip radius, taking into account roughness of the substrate. Reproduced from reference.[82]

interactions on a nearly single molecule basis. Unfortunately, the full potential of these probes has yet to be realized, mostly due to the experimental challenges in the mass production of such probes.

3.2.2 Applied Load and Measured Adhesion Values

The main weakness of CFM, as well as all other AFM-based adhesion measurement techniques, is its inability to obtain an independent measure of the contact area. Frequently, a tip-sample friction force is assumed to provide a simultaneous measurement of the contact area on the assumption that friction is proportional to the actual contact area and interfacial shear stress for corresponding functional group pairs.[86]

$$F = \tau_0 \pi a^2 \tag{21}$$

Note that the general relationship between the radius of the area of contact and the external load (Equation 12) predicts a nonlinear relationship between friction force and applied load. Surprisingly, most of the reported experimental friction-load curves in chemical force microscopy showed approximately linear behavior.[26, 87–90] Vezenov et al.[35] attributed the apparent linear shape of these curves to the averaging of multiple single-asperity contacts that occurs when a friction force is averaged over a path of several micrometers in a typical

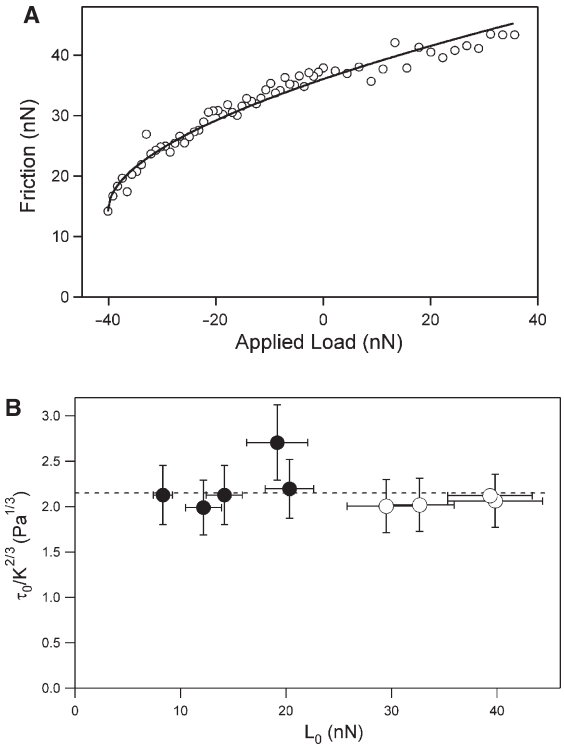

Figure 9. (A) Friction force versus applied load curve (o) for a CH_3 terminated tip and sample in water. The shape of the curve is consistent with the nonlinear dependence of the contact area on external load predicted by the JKR model (fit). (B) Interfacial shear strength, τ_0, of methyl-methyl contacts in methanol-water mixtures normalized by the elastic constant, $K^{2/3}$, plotted versus the force of adhesion measured simultaneously. Closed and open symbols represent different experiments.[91]

friction measurement. The nonlinear JKR-like behavior was detectable only for relatively blunt tips when large forces for hydrophobic SAMs in water turned substrate imperfections into secondary effects (Figure 9A). Nonlinear relationships were also observed between friction and applied load in methanol-water mixtures using methyl terminated siloxane SAMs on smooth Si substrates and silicon nitride tips (Figure 9B).[35] For the same tip-sample pair, the adhesion increased with higher water content; however, the interfacial shear stress, determined by fitting to a contact mechanics model, remained constant.

3.2.3 Adhesion and the Surface Free Energy: Systematic Variations of Adhesion in Mixed Solvent and Mixed SAM Systems

A fruitful strategy to test the scaling relationship between the adhesion forces and the interfacial free energies predicted by the contact mechanics theories for quasi-equilibrium unbinding is to use the same tip and sample pair and vary either the solvent composition or the SAM composition on the probe. This arrangement preserves the geometrical parameters of the system while varying the interfacial free energies of the interacting system in a smooth and predictable manner. For example, Vezenov et al. used the same tip-sample pair terminating in CH_3 groups to determine adhesion forces in a series of methanol-water mixtures.[91] These measurements produced an unambiguous linear correlation between adhesion forces and corresponding surface free energy values determined from independent contact angle

measurements, thus providing an additional corroboration of the scaling relationships predicted in such systems by the contact mechanics models (Figure 10).

3.2.4 Mechanical Properties of Sams and Effect of Chain Packing

The degree of packing in the SAM is affected by the anchoring mechanism and defect density and is generally different for thiolates on Au, trichrolosilanes on Si, and trimethoxysilanes on Si. The tilt angle of alkyl chains with respect to substrate is influenced by the anchoring group density in these SAMs. Thicknesses of these monolayers measured by ellipsometry (2.2 nm, 2.4 nm, and 1.9 nm, respectively) is consistent with an all-trans conformation and an expected trend in tilt angles of 30°, 10°, and 40°, respectively. Most important for the CFM measurements, the orientation of the terminal group is therefore different for these three commonly encountered types of the SAMs. Klein and co-workers performed elegant experiments exploring this degree of freedom in the CFM experiments by measuring adhesion forces between $HS(CH_2)_{17}CH_3$/Au tips and $HS(CH_2)_{17}CH_3$, $Cl_3Si(CH_2)_{17}CH_3$, and $(CH_3O)_3Si(CH_2)_{17}CH_3$ monolayers in water. Adhesion forces were sensitive to SAM internal organization.[92] The adhesion results obtained with three different probes, while nominally reflecting methyl-methyl interactions in water, displayed a trend that paralleled the quality of organization of the SAMs: adhesion forces ratios were $1/(0.797 \pm 0.005)/(0.687 \pm 0.006)$ for HS-, Cl_3Si-, and $(CH_3O)_3Si$-anchor groups, correspondingly (the error is the standard deviation of the mean for different tips). Interestingly, the contact angles, measured on the same series of samples, were much less sensitive to the type of SAMs (111°, 110°, and 108°). Thus, different chain packing and orientation of the terminal group of the self-assembled monolayer can lead to measurable differences in the pull-off forces and thus can serve as a sensitive probe of the conformation of the surface chemical groups. The sensitivity to conformation was also demonstrated by the discrimination of chiral isomers on the basis of adhesion forces detected in CFM experiments.[93] On the other hand, the use of the work of adhesion of a "reference" system, such as methyl-methyl contacts in water ($W = 103\,mJ/m^2$), to determine effective tip radius[33,94] should be used with caution, because nominally the same interface can produce a different apparent work of adhesion depending on the packing of the underlying alkane chain.

3.2.5 Role of the Solvent and Hydrogen Bonding Interactions

Surface free energy arguments explain the magnitudes of adhesion forces measured between organic functional groups in ethanol. Lieber and co-workers observed[91] that adhesion measured by CFM did not correlate with solvent polarity (dipole moment or dielectric constant) or

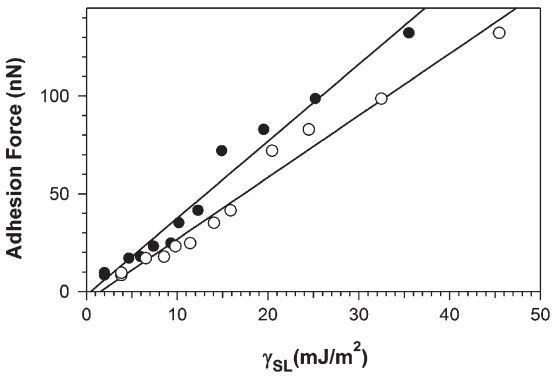

Figure 10. Adhesion between CH_3-terminated tips and samples versus solid-liquid surface free energy determined from advancing (open symbols) and receding (closed symbols) contact angles for CH_3-terminated SAM ($\gamma_{SV} = 19.3\,mJ/m^2$).[91]

cohesion energy. On the other hand, they found[91] that the surface tension component (STC) theory (Section 3.1.3) is generally useful in explaining CFM data in various solvents.

For CH_3-terminated SAMs, the last three terms in Equation 20 are all zero (i.e., $\gamma^{AB} = \gamma^+ = \gamma^- = 0$), while the van der Waals component γ^{LW} determined from contact angle measurements with liquid hydrocarbons (19.3 mJ/m^2) is essentially the same as the corresponding γ^{LW} values for alcohols and water (21.8, 18.5, and 20.1 mJ/m^2 for water, MeOH, and EtOH, respectively). Thus, the first term in Equation 20 is also negligible and the value of the adhesion force between two methyl surfaces in alcohols (or water) is essentially a measure of the strength of the hydrogen bonding interaction (in a free energy sense) in liquid alcohol (water):

$$W_{CH_3/ROH/CH_3} = 2\,\gamma^{AB}{}_{ROH} \quad (R = CH_3CH_2,\ CH_3 \text{ or H}) \tag{22}$$

Ethanol and methanol have indistinguishable values of surface tension (22.8 and 22.6 mJ/m^2, respectively) but different hydrogen bonding components (γ^{AB} = 2.7 and 4.1 mJ/m^2, respectively), both of which are much smaller than the corresponding value for water (γ^{AB} = 51 mJ/m^2). When the same tip and sample are used in the adhesion experiment, forces between CH_3 groups in MeOH were consistently 1.5–2 times greater than those in EtOH, in agreement with the ratio of 1.6 between corresponding γ^{AB} values. Clear and Nealey measured adhesion forces between $HS(CH_2)_{17}CH_3$ modified Au-coated probes and CH_3- and COOH-terminated siloxane monolayers on Si substrates.[94] For a number of solvents (hexadecane, ethanol, propanediols, and water), they also found a good agreement between the work of adhesion for CH_3/CH_3 interface (i) obtained experimentally with CFM, (ii) predicted form contact angle measurements, and (iii) the values calculated from the STC model.

Ethylene glycol (EG) and dimethylsulfoxide (DMSO) present another example of two solvents with a similar surface tension (48 and 44 mJ/m^2) but quite different adhesion forces between apolar surfaces. These solvents have significant acid-base components (19 and 8 mJ/m^2, respectively) and dispersion contributions that differ from that of the CH_3-terminated SAM (29 and 36 mJ/m^2, respectively). Adhesive forces between methyl surfaces in EG are predicted (Equation 20) to be greater than those in DMSO by a factor of 1.8, while experiments yielded a factor of 1.8–2.0 difference.[91] These data independently confirm the validity of the intermolecular force components approach for treating adhesive interactions between organic groups in liquid medium.

The methanol-water mixture provided a simple way to generate similar solvents that spanned a large range of hydrogen bonding ability (γ^{AB} = 4 to 51 mJ/m^2). With a nonpolar SAM, the force of adhesion increased monotonically in mixed solvents of higher water content; whereas, with a SAM having a hydrogen bonding component (COOH groups), higher water content led to decreased adhesion compared to the nonpolar counterpart. Overall, surface tension component interpretation of the CFM data in solvents showed that competition between hydrogen bonding *within the solvent* and hydrogen bonding *between surface groups and the solvent* provided the main contribution to adhesion forces between organic functional groups in liquids. Water, with its exceptional hydrogen bonding properties (both as acceptor and donor), used as a solvent in CFM measurements will therefore discriminate best between various organic groups.

Liquids that form strong interfacial bonds can display two adhesion minima: (i) one corresponding to contact between the groups of the tip and the first solvation shell of the surface when the maximum load on the tip in contact is small, and (ii) the second, deeper, minimum corresponding to contact between the tip and the surface groups when the maximum load is high and the solvation shell is fully penetrated. For OH-OH pair in octanol, the CFM gives γ_{SL} = 0.16 mJ/m^2 and 0.60 mJ/m^2, respectively, for the two minima.[95]

A set of interesting experiments involves COOH and OH groups in both nonpolar and hydrogen bonding solvents. The acid-base components of surface free energy of these SAMs are not readily available from contact angle measurements, because most test liquids will

completely wet such surfaces. The CFM in these systems can potentially provide, along with a dispersion γ^{LW} component, the values of γ^+ and γ^- which together will completely characterize adhesion between these SAMs and other organic surfaces. For example, STC treatment[95] of $W_{OH/HD/OH}$ and $W_{OH/HD/CH3}$ values (HD is hexadecane) using Equation 20 yields $\gamma^{AB}{}_{OH} \approx 1.1\text{-}1.5\,mJ/m^2$. On the other hand, one would obtain $\gamma^{AB}{}_{OH} \approx 24.6\,mJ/m^2$ for the same monolayers when using values of the work of adhesion $W_{OH/HOH/OH}$ and $W_{OH/HOH/CH3}$ found with CFM in water. Warszynski et al. argued[95] that the discrepancy can be resolved if one assumes that in a combining relationship (Equation 19) one needs to take the values for surface free energy of solids saturated with the respective liquids. Rearrangement of surface groups in response to different environments is another possible factor responsible for changingthe γ^{AB} component of the SAM. In addition, the STC model has been shown to have internal inconsistencies, and CFM could be a powerful tool to provide estimates of surface tension components directly for each individual solvent/surface pair. Clearly, the γ^{AB} values for high surface energy groups are not available by other means; in these situations, CFM can be used as an independent method to construct the respective acid-base scales.

4 Kinetic Effects in CFM Measurements

4.1 Chemical Force Microscopy in the Kinetic Regime

So far we have concentrated on the scaling behaviors described by the thermodynamic models of chemical force microscopy. Yet, since CFM typically probes the interactions of a very small number of individual molecular contacts, the thermal fluctuations are still significant, and thus they should exhibit some elements of the bond rupture kinetics typical for non-equilibrium forced unbinding of single bonds. These effects are discussed in detail in the other chapters, so here we provide only a very cursory sketch, mostly for the sake of consistency. If the interacting system is loaded at a very high rate, such that the bond rupture occurs far from equilibrium, the applied force would exponentially amplify the kinetic rate of dissociation. As solved by Evans and Ritchie,[96] the kinetic equations for the case of linear loading (as encountered in the AFM experiments) predict that the pull-off force at constant loading rate r_f is:[97]

$$f_{pull\text{-}off} = \frac{k_B T}{x_\beta} \ln\left(\frac{r_f}{r_0}\right) \tag{23}$$

Characteristic loading rate r_0 is defined as:

$$r_0 = \frac{k_B T}{x_\beta} \cdot \frac{1}{\tau_D \exp\left(\frac{E_0}{k_B T}\right)}$$

where τ_D represents the inverse of the diffusion-limited attempt frequency, E_0 is the depth of the energy well, and x_β is the distance to the transition state.

Direct application of this formalism to the CFM experiment presents several significant challenges. CFM almost always involves the rupture of multiple individual bonds connected in parallel. Williams and Evans considered the kinetics of the bond rupture in such systems[98, 99] and showed that the kinetics of bond rupture is nontrivial in the general case of uncorrelated bonds. However, the analysis could be simplified by assuming that all the bonds are correlated, i.e., they share a single reaction coordinate. Then the system could represent a single "macro-bond" with the total potential equal to the sum of the potentials of individual components.[99] For the serial loading of N identical bonds Williams and Evans obtained the following expression for the unbinding force:

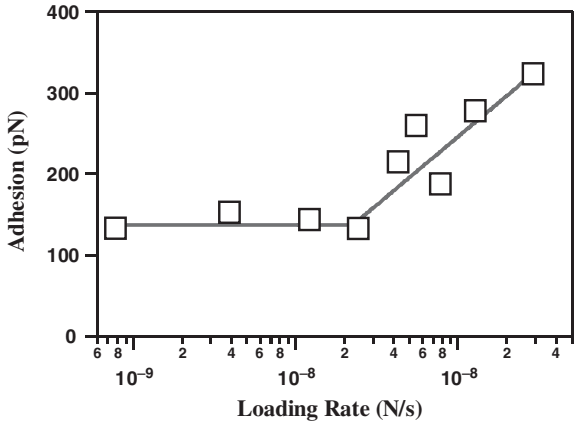

Figure 11. Binding forces between COOH-modified probe and sample in ethanol plotted as a function of loading rate.[34] Lines indicate fits according to Equation 25 in the equilibrium and nonequilibrium unbinding regimes.

$$f_{pull-off} = \frac{k_B T}{x_\beta} \ln\left(\frac{r_f}{r_0} N \exp\left(\frac{(N-1)E}{k_B T}\right)\right) \tag{24}$$

Qualitatively, in the case of such parallel loading of N bonds, the binding force is only slightly smaller than N times single bond strength (yet the scaling is not exact!). Another important feature of this case is that the distance scale of the interactions is unchanged, i.e., the width of the potential for the "macro-bond" is still equal to the width of the potential for a single bond. Moreover, the scaling of the bond strength with the loading rate predicted by the kinetic model for a single bond case is still valid.

Configuration constraints imposed by the rigid self-assembled monolayers provide an almost ideal parallel loading case; therefore, we can use the CFM measurements in the kinetic regime to determine the width of the interaction potential. Noy and coworkers[34] tested this regime for the interactions of COOH-terminated surfaces (Figure 11) and observed the behavior predicted by the kinetic analysis. When the tip-sample junction was loaded slowly, the unbinding force was virtually independent of the loading rate, indicating unbinding in the equilibrium regime. As the loading rate increased further, the system transitioned to the nonequilibrium unbinding and started to exhibit a characteristic exponential increase in the binding force with the loading rate. The measured slope of this increase estimates the distance to the transition state as 0.6 Å for the interactions between COOH functionalities. The distance to the transition state is significantly shorter than the values typically observed for interactions between biological macromolecules (see the Chapters 5 and 8), which is reasonable to expect considering the size difference. Interestingly, this value is comparable to the barrier width *per base pair* (0.7Å) obtained by Strunz et al. in the DNA unbinding experiments.[100] It is tempting to assign the value obtained in these measurements to the hydrogen bond potential, but, as we will show in the next section, the real picture is more complicated.

4.2 Probing Entropic Barriers in Nanoscale Adhesion with CFM

As we have discussed in Section 2, solvation plays a very important role in shaping the interactions between chemically-modified probes and surfaces. The surface tension component model provides the quantitative framework for predicting binding forces in the near-equilibrium regime. However, we can gain a deeper understanding of the origin of such forces

if we consider the temperature dependence of the tip-sample interaction strength. Noy and co-workers[34, 36] studied the strength of the interactions between several different surfaces as a function of temperature. Intuitively, we expect the binding force to decrease as the temperature increases and the thermal fluctuations gain more energy to break the bond. Surprisingly, the researchers observed (Figure 12) that for interactions between COOH-terminated surfaces in a polar, hydrogen-bonding solvent the interaction strength *increased* with the temperature.[36] This behavior was also present for interactions of other hydrophilic functionalities in polar solvents. Conversely, when the liquid medium was switched to a nonpolar solvent (hexane) the temperature trend reversed. The researchers attributed this behavior to the large negative entropy accompanying ordering of solvent molecules at the interfaces.[36] This negative entropy destabilizes the unbound state and leads to the observed counterintuitive temperature dependence. Nonpolar solvents do not tend to form ordered layers and thus do not contribute to these *entropic* solvation barriers.

The kinetic model outlined in the previous section can provide a quantitative interpretation of this phenomenological picture. If we separate the energy barrier into enthalpic and entropic components, $E_0 = \Delta H - T\Delta S$, and substitute Equation into Equation we can represent the temperature dependence of pull-off forces in the following form:

$$f_{pull-off} = \frac{\Delta H}{x_\beta} - \frac{\Delta S}{x_\beta} T - \frac{k_B T}{x_\beta} \ln\left[\frac{k_B T}{r_f \tau_D x_\beta}\right]. \tag{25}$$

The first two terms in Equation 25 describe the enthalpic and the entropic contribution to the bond strength, and the third term describes the contribution of thermal motion to the bond strength. In other words, the first two components describe the true energy-barrier

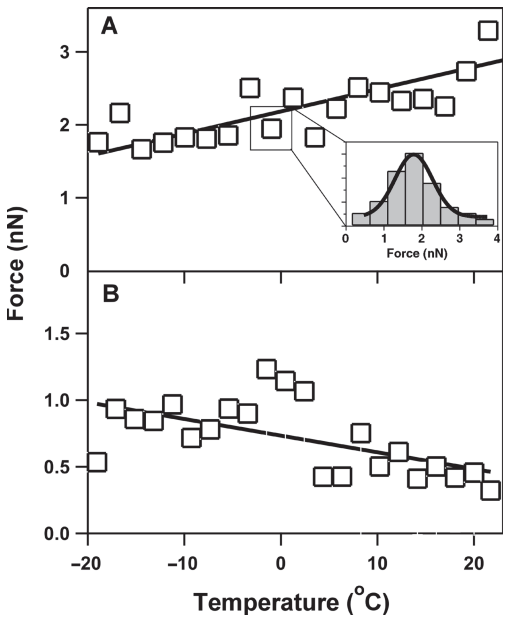

Figure 12. (A) Binding force as a function of temperature for interactions of COOH-modified probe and sample in ethanol. Inset shows a binding force histogram at one temperature point. (B) Binding force as a function of temperature for the interactions of COOH-modified probe and sample in hexane.

contribution and the (always negative) third component describes the "thermal weakening" of a bond caused by the thermal fluctuations helping the system to get over the activation barrier.

Equation 25 highlights another bit of nontrivial physics of the behavior of intermolecular bonds under external load. The third term in Equation 25 ("thermal weakening") always increases in magnitude as the temperature increases, leading to the overall decrease in the observed force, in full agreement with the intuitive picture. Yet the entropic term can lead to either increase or decrease in the overall interaction force depending on the sign on the entropy change for the unbinding process. Therefore, for the cases when the energy barrier has a large entropy component (i.e., in cases of associating solvents and high surface energy groups), we expect the bond strength to increase with the temperature. The relative magnitude of the entropic and the kinetic terms in Equation 25 defines two regimes of bond rupture: (i) thermally-dominated kinetics, where the kinetic weakening leads to a decrease in the observed bond strength with the increase in temperature; and (ii) barrier-dominated kinetics, where the entropic term overwhelms the kinetic term and leads to an increase in interaction strength with the increase in temperature. Furthermore, Equation 25 also indicates that the entropic regime of unbinding must exist only over a limited range of temperatures. As the temperature increases, the kinetic term, which increases as $T \cdot lnT$, will overwhelm the entropic term, which increases only linearly. For the entropic forces caused by the ordering of the solvent molecules at the surface, this crossover point simply corresponds to the situation when the thermal motion overwhelms molecular ordering in the solvent layers in the vicinity of the surface.

5 Conclusions

The chemical force microscopy approach provides several remarkable opportunities for force spectroscopy of specific intermolecular interactions. First, this technique creates a nanoscale tool that can address directly the roles that the different chemical functionalities, the nature of the solvent, and environmental variables play in shaping the strength of intermolecular interactions. Second, CFM studies go beyond the naïve notion that intermolecular interaction strength is determined solely by the nature of the interacting groups, and thus can be used as a universal tool for chemical identification. Indeed, CFM studies show that the interaction strength between two chemical species always reflects not only the nature of the species, but also the context of the environment surrounding these species, and in particular the solvent medium, which always plays a critical role in shaping intermolecular interactions in condensed phases.

Despite these complications, practical realizations of chemical force microscopy have shown tremendous progress towards understanding intermolecular interactions on the molecular level. The studies described in this chapter reveal the central role interfacial free energies play in determining the magnitudes of the observed adhesion (and friction) forces. Continuum contact mechanics models also provide a robust framework for quantitative understanding of the CFM results. We want to emphasize that a quantitative approach to the CFM experiments is almost always necessary to realize the full potential of the technique. Thus it is imperative to use the versatile arsenal of calibration and characterization tools that has been developed for the CFM experiments since the time of the inception of this technique.

Recently, an emerging kinetic view of intermolecular interactions has led to another paradigm shift for understanding these interactions. The kinetic model shows that the measured interaction strength depends not only on the energy landscape of the system, but also on the loading history prior to the bond breakup. This new paradigm refocuses our attention on the energy landscape as a fundamental characteristic of the interaction. Moreover, force spectroscopy approaches derived from the kinetic model allow direct characterization of the potential energy barrier geometry. These developments are only an indication of the rich opportunities

that lie ahead, and chemical force microscopy studies will continue to reveal a true picture of the energy landscapes in complex chemical and biological systems.

References

1. Binnig, G.; Quate, C. F.; Gerber, C. *Phys. Rev. Lett*. **1986**, *56*, 930–3.
2. Quate, C. *Surf. Sci*. **1994**, *299/300*, 980.
3. Smith, D. P. E. *Rev. Sci. Instr*. **1995**, *66*, 3191–5.
4. Frisbie, C. D.; Rozsnyai, L. F.; Noy, A.; Wrighton, M. S.; Lieber, C. M. *Science* **1994**, *265*, 2071.
5. Albrecht, T. R.; Akamine, S.; Carver, T. E.; Quate, C. F. *J. Vac. Sci. Technol. A, Vac. Surf. Films* **1990**, *8*, 3386–96.
6. Meyer, G.; Amer, N. M. *Appl. Phys. Lett*. **1988**, *53*, 1045–7.
7. Cleveland, J. P.; Schaffer, T. E.; Hansma, P. K. *Phys. Rev. B* **1995**, *52*, R8692–R8695.
8. Israelachvili, J. *Intermolecular and Surface Forces*. Academic Press: New York, 1992.
9. Grandbois, M.; Beyer, M.; Rief, M.; Clausen-Schaumann, H.; Gaub, H. E. *Science* **1999**, *283*, 1727–1730.
10. Burnham, N. A.; Colton, R. J.; Pollock, H. M. *J. Vac. Sci. Technol. A, Vac. Surf. Films* **1991**, *9*, 2548–56.
11. Schaffer, T.; Viani, M.; Walters, D.; Drake, B.; Runge, E.; Cleveland, J.; Wendman, M.; Hansma, P. In *Micromachining and Imaging*; SPIE: San Jose, CA, 1997; Vol. 3009, p 48–52.
12. Viani, M. B.; Schaffer, T. E.; Chand, A.; Rief, M.; Gaub, H. E.; Hansma, P. K. *J. Appl. Phys*. **1999**, *86*, 2258–62.
13. Israelachvili, J. *Acc. Chem. Res*. **1987**, *20*, 415–21.
14. Chaudhury, M. K.; Whitesides, G. M. *Langmuir* **1991**, *7*, 1013–25.
15. Chaudhury, M. K.; Whitesides, G. M. *Science* **1992**, *255*(*5049*), 1230–2.
16. Kappl, M.; Butt, H. J. *Particle & Particle Systems Characterization* **2002**, *19*, 129.
17. Ducker, W. A.; Senden, T. J.; Pashley, R. M. *Nature* **1991**, *353*, 239–241.
18. Houston, J. E.; Michalske, T. A. *Nature* **1992**, *356*, 266–267.
19. Bustamante, C.; Macosko, J. C.; Wuite, G. J. L. *Nature Reviews Molec. Cell Biol*. **2000**, *1*, 130–136.
20. Nuzzo, R. G.; Allara, D. L. *J. Am. Chem. Soc*. **1983**, *105*, 4481.
21. Porter, M. D.; Bright, T. B.; Allara, D. L.; Chidsey, C. E. D. *J. Am. Chem. Soc*. **1987**, *109*, 3559–3568.
22. Bain, C. D.; Troughton, E. B.; Tao, Y.-T.; Evall, J.; Whitesides, G. M.; Nuzzo, R. G. *J. Am. Chem. Soc*. **1989**, *111*.
23. Bain, C. D.; Evall, J.; Whitesides, G. M. *J. Am. Chem. Soc* **1989**, *111*, 7155.
24. Bain, C.; Whitesides, G. *Angew. Chem. Int. Ed. Engl*. **1989**, *28*, 506–512.
25. Whitesides, G. M.; Laibinis, P. E. *Langmuir* **1990**, *6*, 87.
26. Noy, A.; Frisbie, C. D.; Rozsnyai, L. F.; Wrighton, M. S.; Lieber, C. M. *J. Am. Chem. Soc*. **1995**, *117*, 7943–7951.
27. Vezenov, D. V.; Noy, A.; Rosznyai, L. F.; Lieber, C. M. *J. Am.Chem. Soc*. **1997**, *119*, 2006–2015.
28. Noy, A.; Sanders, C. H.; Vezenov, D. V.; Wong, S. S.; Lieber, C. M. *Langmuir* **1998**, *14*, 1508–1511.
29. Nakagawa, T.; Ogawa, K.; Kurumizawa, T.; Ozaki, S. *Japanese J. Appl. Phys., Part 2 (Letters)* **1993**, *32*, L294–6.
30. Nakagawa, T.; Ogawa, K.; Kurumizawa, T. *J. Vac. Sci. Technol. B, Microelectron. Nanometer Struct*. **1994**, *12*, 2215–18.
31. Green, J.-B. D.; McDermott, M. T.; Porter, M. D.; Siperko, L. M. *J. Phys.Chem*. **1995**, *99*, 10960.
32. Thomas, R. C.; Tangyunyong, P.; Houston, J. E.; Michalske, T. A.; Crooks, R. M. *J. Phys. Chem*. **1994**, *98*, 4493.
33. Sinniah, S. K.; Steel, A. B.; Miller, C. J.; Reutt-Robey, J. E. *J. Am. Chem. Soc*. **1996**, *118*, 8925–8931.
34. Zepeda, S.; Yeh, Y.; Noy, A. *Langmuir* **2003**, *19*, 1457–1461.
35. Vezenov, D. V.; Noy, A.; Lieber, C. M. *J. Adhes. Sci.Tech*. **2003**, *17*, 1385–1401.
36. Noy, A.; Zepeda, S.; Orme, C. A.; Yeh, Y.; De Yoreo, J. J. *J. Am. Chem. Soc*. **2003**, *125*, 1356 – 1362.
37. Noy, A.; Huser, T. R. *Rev. Sci. Instr*.**2003**, *74*, 1217–1221.
38. Xiao, X.; Qian, L. *Langmuir* **2000**, *16*, 8153–8158.
39. Jang, J.; Schatz, G. C.; Ratner, M. A. *J. Chem. Phys*. **2004**, *120*, 1157–1160.
40. Wilbur, J. L.; Biebuyck, H. A.; MacDonald, J. C.; Whitesides, G. M. *Langmuir* **1995**, *11*, 825–831.
41. Poggi, M. A.; Bottomley, L. A.; Lillehei, P. T. *Nano Lett*. **2004**, *4*, 61–64.
42. Drake, B.; Prater, C. B.; Weisenhorn, A. L.; Gould, S. A. C.; Albrecht, T. R.; Quate, C. F.; Cannell, D. S.; Hansma, H. G.; Hansma, P. K. *Science* **1989**, *243*, 1586–9.
43. Fotiadis, D.; Scheuring, S.; Muller, S. A.; Engel, A.; Muller, D. J. *Micron* **2002**, *33*, 385–397.
44. Malkin, A. J.; Land, T. A.; Kuznetsov, Y. G.; McPherson, A.; Deyoreo, J. J. *Phys.l Rev. Lett*. **1995**, *75*, 2778–2781.

45. Land, T. A.; Malkin, A. J.; Kuznetsov, Y. G.; McPherson, A.; Deyoreo, J. J. *Phys.l Rev. Lett*. **1995**, *75*, 2774–2777.
46. Kuznetsov, Y. G.; Malkin, A. J.; McPherson, A. *J. Cryst. Growth* **1999**, *196*, 489–502.
47. Kuznetsov, Y. G.; Malkin, A. J.; Land, T. A.; DeYoreo, J. J.; Barba, A. P.; Konnert, J.; McPherson, A. *Biophys. J*.**1997**, *72*, 2357–2364.
48. Malkin, A. J.; Kuznetsov, Y. G.; Lucas, R. W.; McPherson, A. *J. Struct. Biol*. **1999**, *127*, 35–43.
49. Li, M. Q. *Appl. Phys. A:* **1999**, *68*, 255–258.
50. Woolley, A. T.; Cheung, C. L.; Hafner, J. H.; Lieber, C. M. *Chemistry & Biology* **2000**, *7*, 193–204.
51. Noy, A.; Vezenov, D.; Kayyem, J.; Meade, T.; Lieber, C. *Chemistry & Biology* **1997**, *4*, 519–527.
52. Friddle, R.; Klare, J. E.; Martin, S.; Corzett, M.; Balhorn, R.; Baldwin, E. P.; Baskin, R.; Noy, A. *Biophys. J*. **2004**, *86*, 1632–1639.
53. Sulchek, T. A.; Friddle, R. W.; Langry, K.; Lau, E. Y.; Albrecht, H.; Ratto, T. V.; DeNardo, S. J.; Colvin, M. E.; Noy, A. *Proc. Natl. Acad. Sci. USA* **2005**, *102*, 16638–16643.
54. Kienberger, F.; Ebner, A.; Gruber, H. J.; Hinterdorfer, P. *Acc. Chem. Res* **2006**, *39*, 29–36.
55. Cleveland, J. P.; Manne, S.; Bocek, D.; Hansma, P. K. *Rev. Sci. Instr*. **1993**, *64*, 403–5.
56. Hutter, J. L.; Bechhoefer, J. *Rev. Sci. Instr*. **1993**, *64*, 1868–73.
57. Sader, J. E.; Larson, I.; Mulvaney, P.; White, L. R. *Rev. Sci. Instr*. **1995**, *66*, 3789–98.
58. Sader, J. E.; Chon, J. W. M.; Mulvaney, P. *Rev. Sci. Instr*. **1999**, *70*, 3967–9.
59. Ogletree, D. F.; Carprick, R. W.; Salmeron, M. *Rev. Sci. Instr*. **1996**, *67*, 3298.
60. Warmack, R. J.; Zheng, X. Y.; Thundat, T.; Allison, D. P. *Rev. Sci. Instr*. **1994**, *65*, 394–9.
61. Neumeister, J. M.; Ducker, W. A. *Rev. Sci. Instr*. **1994**, *65*, 2527–31.
62. Hazel, J. L.; Tsukruk, V. V. *Thin Solid Films* **1999**, *339*, 249–57.
63. Marti, O. *Phys. Scr. Vol. T (Sweden), Physica Scripta Volume T* **1993**, *T49B*, 599–604.
64. D'Costa, N. P.; Hoh, J. H. *Rev.f Sci. Instr*. **1995**, *66*, 5096–7.
65. Liu, Y.; Wu, T.; Fennel-Evans, D. *Langmuir* **1994**, *10*, 2241.
66. Liu, Y. H.; Evans, D. F.; Song, Q.; Grainger, D. W. *Langmuir* **1996**, *12*, 1235–1244.
67. Schwarz, U. D.; Koster, P.; Wiesendanger, R. *Rev. Sci. Instr*. **1996**, *67*, 2560–7.
68. Thomas, R. C.; Houston, J. E.; Crooks, R. M.; Kim, T.; Michalske, T. A. *J. Am. Chem. Soc*. **1995**, *117*, 117.
69. Derjaguin, B. V.; Muller, V. M.; Toporov, Y. P. *J. Coll. Interf. Sci*. **1975**, *53*, 314–26.
70. Carpick, R. W.; Agrait, N.; Ogletree, D. F.; Salmeron, M. *J. Vac. Sci. Technol. B, Microelectron. Nanometer Struct*. **1996**, *14*, 1289–95.
71. Muller, V. M.; Yushchenko, V. S.; Derjaguin, B. V. *J. Coll. Interf. Sci*. **1980**, *77*, 91–101.
72. Maugis, D. *Langmuir* **1995**, *11*, 679–682.
73. Carpick, R. W.; Sasaki, D. Y.; Burns, A. R. *Tribology Letters* **1999**, *7*, 79–85.
74. Johnson, K. L. *Proc. Roy.l Soc., London, A* **1997**, *453*, 163–179.
75. Dzyaloshinskii, I. E.; Lifshitz, E. M.; Pitaevskii, L. P. *Physics-Uspekhi* **1961**, *4*, 153–176.
76. London, F. *Trans. Faraday Soc* **1937**, *33*, 10.
77. van Oss, C. J.; Chaudhury, M. K.; Good, R. J. *Chem. Rev*. **1988**, *88*, 927–41.
78. Segeren, L.; Siebum, B.; Karssenberg, F. G.; Van Den Berg, J. W. A.; Vancso, G. J. *J. Adh. Sci. Technol*. **2002**, *16*, 793–828.
79. McKendry, R.; Theoclitou, M.; Abell, C.; Rayment, T. *Langmuir* **1998**, *14*, 2846–2849.
80. Sato, F.; Okui, H.; Akiba, U.; Suga, K.; Fujihira, M. *Ultramicroscopy* **2003**, *97*, 303–14.
81. Williams, P. M. *Analytica Chim. Acta* **2003**, *479*, 107–115.
82. Skulason, H.; Frisbie, C. D. *Langmuir* **2000**, *16*, 6294–6297.
83. Wong, S. S.; Joselevich, E.; Woolley, A. T.; Cheung, C. L.; Lieber, C. M. *Nature* **1998**, *394*, 52–55.
84. Hafner, J. H.; Cheung, C. L.; Lieber, C. M. *J. Am. Chem. Soc*. **1999**, *121*, 9750–9751.
85. Hafner, J. H.; Cheung, C. L.; Oosterkamp, T. H.; Lieber, C. M. *J. Phys. Chem. B* **2001**, *105*, 743–746.
86. Caprick, R.; Salmeron, M. *Chem. Rev*. **1997**, *97*, 1163–1194.
87. Beake, B. D.; Leggett, G. J.; Shipway, P. H. *Surf. Interf. Analysis* **1999**, *27*, 1084–1091.
88. Brewer, N. J.; Leggett, G. J. *Langmuir* **2004**, *20*, 4109–4115.
89. Leggett, G. J.; Brewer, N. J.; Chong, K. S. L.; Matter, S. *Phys. Chem. Chem. Phys* **2005**, *7*, 1107–1120.
90. Brewer, N. J.; Foster, T. T.; Leggett, G. J.; Alexander, M. R.; McAlpine, E. *J Phys. Chem. B*, **2004**, *108*, 4723–4728.
91. Vezenov, D. V.; Zhuk, A. V.; Whitesides, G. M.; Lieber, C. M. *J. Am. Chem. Soc*. **2002**, *124*, 10578–10588.
92. Duwez, A. S.; Jonas, U.; Klein, H. *Chem. Phys. Chem*. **2003**, *4*, 1107–1111.
93. Mckendry, R.; Theoclitou, M.; Rayment, T.; Abell, C. *Nature* **1998**, *391*, 566–568.
94. Clear, S. C.; Nealey, P. F. *J. Coll. Interf. Sci*. **1999**, *213*, 238–250.
95. Warszynski, P.; Papastavrou, G.; Wantke, K. D.; Mohwald, H. *Colloids and Surfaces A: Physicochemical and Engineering Aspects* **2003**, *214*, 61–75.
96. Evans, E.; Ritchie, K. *Biophys. J*. **1997**, *72*, 1541–1555.

97. Evans, E. *Faraday Discussions* **1999**, 1–16.
98. Evans, E.; Williams, P. In *Physics of Bio-Molecules and Cells*; Flyvbjerg, H., Jülicher, F., Ormos, P., David, F., Eds.; Springer and EDP Sciences: Heidelberg, 2002; Vol. 75, p 147–185.
99. Evans, E.; Williams, P. In *Physics of Bio-Molecules and Cells*; Flyvbjerg, H., Jülicher, F., Ormos, P., David, F., Eds.; Springer and EDP Sciences: Heidelberg, 2002; Vol. 75, p 187–203.
100. Strunz, T.; Oroszlan, K.; Schafer, R.; Guntherodt, H. J. *Proc. Natl. Acad. Sci. U.S.A*. **1999**, *96*, 11277–11282.
101. Han, T.; Williams, J. M.; Beebe, T. P., Jr. *Anal. Chim. Acta* **1995**, *307*, 365–376.
102. Ito, T.; Namba, M.; Buehlmann, P. and Umezawa, Y. Langmuir, **1997**, *13*, 4323–4332.
103. Headrick, J. E. and Berrie, C. L. Langmuir, **2004**, *20*, 4124–4131.
104. Ara, M. and Tada, H. *Appl. Phys. Lett*. **2003**, *83*, 578–580.
105. Vezenov, D. V.; Noy, A.; Ashby, P. J. *Adh. Sci. Tech*. **2005**, *19*, 313–364.
106. Tormoen, G. W.; Drelich, J.; Beach, E. R., J. *Adh. Sci. Tech*. **2004**, *18*, 1–17.